Reynolds number effects on Rayleigh–Taylor instability with possible implications for type-Ia supernovae

WILLIAM H. CABOT* AND ANDREW W. COOK*

Lawrence Livermore National Laboratory, 7000 East Ave., Livermore, California 94550-9234, USA

*e-mail: cabot1@llnl.gov; awcook@llnl.gov

Published online: 23 July 2006; doi:10.1038/nphys361

Spontaneous mixing of fluids at unstably stratified interfaces occurs in a wide variety of atmospheric, oceanic, geophysical and astrophysical flows. The Rayleigh–Taylor instability, a process by which fluids seek to reduce their combined potential energy, plays a key role in all types of fusion. Despite decades of investigation, fundamental questions regarding turbulent Rayleigh–Taylor flow persist, namely: does the flow forget its initial conditions, is the flow self-similar, what is the scaling constant, and how does mixing influence the growth rate? Here, we show results from a large direct numerical simulation addressing such questions. The simulated flow reaches a Reynolds number of 32,000, far exceeding that of all previous Rayleigh–Taylor simulations. We find that the scaling constant cannot be found by fitting a curve to the width of the mixing layer (as is common practice) but can be obtained by recourse to the similarity equation for the expansion rate of the turbulent region. Moreover, the ratio of kinetic energy to released potential energy is not constant, but exhibits a weak Reynolds number dependence, which might have profound consequences for flame propagation models in type-Ia supernova simulations.

Rayleigh–Taylor instabilities (RTIs) arise from baroclinic generation of vorticity at a perturbed interface subject to acceleration in a direction opposite the mean density gradient[1,2]. RTI plays a crucial role in all known forms of fusion, whether the confinement be magnetic[3], inertial[4,5] or gravitational[6]. Regarding gravitational fusion, much work over recent years points to Rayleigh–Taylor-driven turbulence as the dominant acceleration mechanism for thermonuclear flames in type-Ia supernovae[7]. In addition to producing many intermediate-mass elements, type-Ia supernovae serve as standard candles for measuring the rate of expansion of the universe. They begin as carbon–oxygen white dwarfs, which accrete mass from a companion star. When the mass of the white dwarf reaches the Chandrasekhar limit of 1.4 solar masses, ignition occurs near the centre, thus generating a thermonuclear flame front. The expansion of ashes behind the front causes the flame to become Rayleigh–Taylor unstable as it propagates outwards.

A major difficulty in supernova modelling is the need to cover the vast dynamic range associated with high Reynolds number turbulence. The thermonuclear flame varies in thickness, from $\sim 10^{-4}$ to ~ 1 cm (ref. 8), whereas the initial radius of a white dwarf is $\sim 10^{8}$ cm; hence, a direct numerical simulation (DNS) of the event would require a grid spanning 12 orders of magnitude in scale. In modern calculations, resolution limitations dictate a numerical flame thickness of $\sim 10^{6}$ cm (refs 9,10). As RTI grows up from scales far below the grid spacing, subgrid-scale (SGS) models must do more than assume a pre-existing Kolmogorov cascade (wherein stationary turbulence already exists above the grid scale) but must be capable of evolving RTI up through 6–10 decades in scale, until the turbulence reaches the grid level. As estimates for the rate of cosmological expansion depend critically on the variability in luminosity of type-Ia events, improved models for RTI are needed to more accurately predict the fate of the universe.

FLOW PHYSICS

For this study, we simplified the physics as much as possible to concentrate all available resources on representing the maximum possible scale range. RTI is a low Mach number

phenomenon[11]; hence, we chose an incompressible formulation to avoid the complicating effect of hydrostatic density variation in the stratified layers. Furthermore, we simulated a non-reacting flow of viscous/diffusive fluids. Our reasoning for this latter choice stems from a subtle connection between reaction and diffusion. For small amplitude perturbations, inviscid linear stability theory[12] predicts an unbounded exponential growth-rate factor for RTIs proportional to the square root of the perturbation wavenumber. However, viscosity and diffusivity inhibit high-wavenumber growth, producing a 'most dangerous' mode, which outpaces all other modes. Diffusion stabilizes the flow above a critical wavenumber, k_D. Including viscous/diffusive effects, the growth factor, n, from linear stability theory is[13]

$$n = \left(gAk/\psi + \nu^2 k^4\right)^{1/2} - (\nu + D)k^2; \qquad (1)$$

where g is gravity,

$$A \equiv \frac{\rho_H - \rho_L}{\rho_H + \rho_L}$$

is the Atwood number (with ρ_L and ρ_H being the densities of the light and heavy fluids, respectively), k is the perturbation wavenumber, ν is the kinematic viscosity, D is the molecular diffusivity and ψ is a function of A, k and the diffusion thickness of the interface, δ. For reacting flows, conductive propagation of a laminar flame 'polishes' small-scale fluctuations, thus stabilizing RTI in a manner roughly analogous to mass diffusion. Timmes and Woosley[14] estimate that wavenumbers greater than gA/S_l^2 are stabilized by the flame in the linear regime, where S_l is the laminar flame speed. For low Schmidt numbers ($\nu < D$) and thin interfaces ($\psi \approx 1$), equation (1) gives a similar result, assuming a correspondence between S_l and $Dk_D = (gAD)^{1/3}$. In the turbulent regime, eddies affect flame propagation when their sizes exceed the Gibson scale, $l(S_l/u')^3$, where u' is the turbulence velocity (root-mean-square of velocity fluctuations about the mean) and l is the inertial length (equation (15)) (ref. 15). We expect that simulations of non-reacting RTI (presented here) and simulations of the reacting case (for example, ref. 7) will exhibit similar behaviour in this flamelet regime, where most of the turbulent energy resides at scales much larger than the diffusive or flame-stabilization scales.

A wide variety of turbulent flows have been observed to reach an asymptotic state only for Reynolds numbers (Re) exceeding 10^4 (ref. 16); our DNS crosses this threshold requirement for strong turbulence. The simulation begins with a thin perturbed planar interface separating light and heavy fluids. Details regarding the simulation are given in the Methods section. Figure 1 shows the turbulent mixing regions that develops after some transitional stages. For the $\rho_H/\rho_L = 3/1$ density ratio of the simulation, downward-moving 'spikes' extend about 20% farther than upward-moving 'bubbles'. Note that very little pure fluid makes it across the middle of the mixing region and almost none reaches all the way through to the other side; that is, there is no red fluid at the very bottom. This picture is qualitatively consistent with type-Ia supernova spectra, which imply that unburnt materials are not transported to the stellar core (assuming centre ignition); that is, Doppler shifts show unburnt carbon and oxygen only at high velocities associated with expanding outer layers[9,17]. Several numerical simulations of type-Ia supernovae have produced convective down-drafts of pure unburnt fuel into the core[9,10]. A possible explanation for this is the manner in which the flame front is initially perturbed. In the early stages of RTI, coherent mushroom-like structures form, engulfing pure fluid and transporting it across the layer for a distance proportional to the wavelength of the initial disturbance. Many 'bubble-merger' generations are required to escape this initial

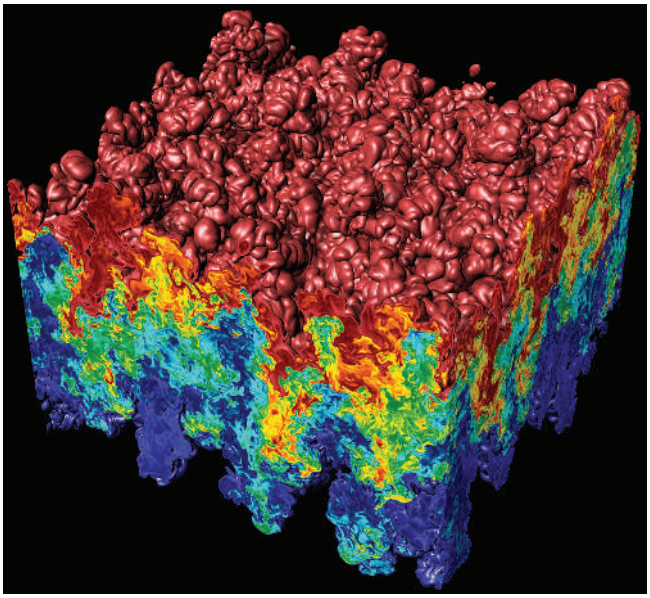

Figure 1 Rayleigh–Taylor instability in the fully turbulent regime. Blue fluid is light (density = 1) and red fluid is heavy (density = 3). The other colours represent mixed fluid of various compositions. The pure fluids above and below the mixing region are not shown. Gravity is directed downwards. The simulation time is $t/\tau = 31$, which corresponds to the end of the calculation.

effect. Hence, simulations with low-wavenumber perturbations (including grid-induced breaking of spherical symmetry) cannot reach an asymptotic self-similar state because the energy spectrum is restricted from developing at the low-wavenumber end.

DYNAMIC RANGE AND THE APPROACH TO ISOTROPY

As the RTI flow evolves, an initial gaussian spectrum of perturbations grows and broadens, eventually developing an inertial range. Figure 2 shows density and velocity spectra at the end of the simulation. As time progresses, the peak of each spectrum moves to lower wavenumbers, whereas the tail (dissipation range) moves to higher wavenumbers; hence, the range of scales participating in the dynamics grows at both ends. The velocity spectra exhibit stronger anisotropy at large scales than at small scales. Zingale *et al.*[7] found similar Kolmogorov spectra with a small-scale tendency towards isotropy in their simulations of RTI thermonuclear flames. The scale-dependence of this anisotropy can be quantified by defining directionally dependent Taylor (equation (17)) and Kolmogorov (equation (18)) microscales. The Taylor scale (λ_i) is the 'smallest large scale' and is associated with the interfacial surface area between the fluids (as will be shown). The Kolmogorov scale (η_i) is the smallest turbulence length scale and is associated with viscous dissipation of kinetic energy; in the DNS we observe $\eta_i \approx \Delta$ at late times, where Δ is the grid spacing.

Defining $h(t)$ as a time-dependent measure of the mixing width (equation (21)), the moment similarity method of Ristorcelli and Clark[18] predicts $\lambda_i \propto h^{1/4} \propto t^{1/2}$ and $\eta_i \propto h^{-1/8} \propto t^{-1/4}$. Our tests of these predictions are plotted in Fig. 3. The DNS confirms the similarity predictions for η_{xy}, η_z and λ_{xy}, but not for λ_z. Ristorcelli and Clark studied Boussinesq ($A \ll 1$) flow where the anisotropy can be neglected. In the non-Boussinesq case, the anisotropic body force is felt at the Taylor microscale, but its effect becomes completely lost at the Kolmogorov scale. This fits well with the classical picture of turbulence, that small scales are more isotropic

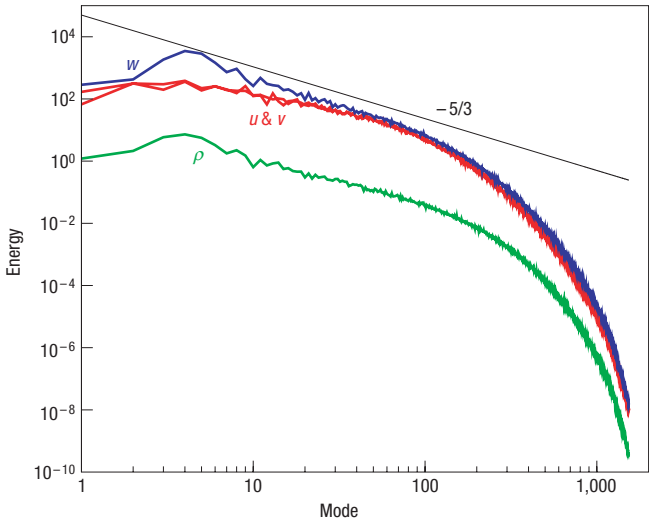

Figure 2 Rayleigh–Taylor energy spectra. Data are from the $z = 0$ plane at $t/\tau = 31$ (end of simulation). The spectra are computed by taking two-dimensional Fourier transforms of density (ρ) and velocity components (u, v, w), multiplying by the complex conjugate and summing over each wavenumber annulus. The mode number is $kL/2\pi$, where k is the wavenumber and L is the size of the numerical domain in the horizontal directions. A fiducial corresponding to Kolmogorov scaling ($k^{-5/3}$) is drawn for reference. The energy spectra are scaled in terms of gravity (g), computational grid spacing (Δ) and the density of the light fluid (ρ_L).

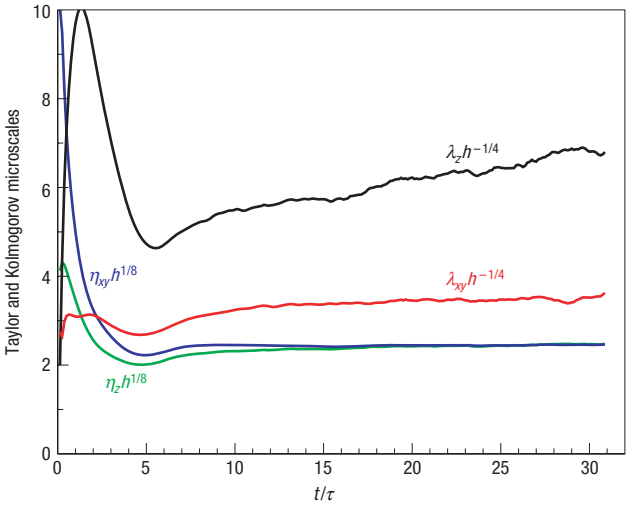

Figure 3 Taylor, $\lambda_i(0, t)$, and Kolmogorov, $\eta_i(0, t)$, microscales normalized by their theoretical dependence on mixing width, $h(t)$. The Kolmogorov microscales eventually become isotropic, whereas the Taylor scales do not. Anisotropy at the Taylor scale increases with Atwood number. All length scales are in units of computational grid spacing (Δ).

than large scales. Whereas the leading fronts of the mixing layer remain anisotropic for all time, the vorticity field behind the fronts evolves from a completely anisotropic state to a completely isotropic state. By examining the ratio of vertical to horizontal vorticity components in the central portion of the mixing layer, we find that complete isotropy is only obtained for $t/\tau > 27$ or Re $>$ 22,000, where τ is a characteristic RTI timescale (equation (16)) and Re is the RTI Reynolds number (equation (23)).

GROWTH RATE

Recently, Ristorcelli and Clark[18] and Cook *et al.*[19], using completely different approaches, derived the same governing equation for h, namely,

$$\dot{h}^2 = 4\alpha A g h, \tag{2}$$

where α is a dimensionless growth parameter. In deriving equation (2), Ristorcelli and Clark used a similarity assumption, whereas Cook *et al.* used a mass flux and energy balance argument. In the Ristorcelli and Clark derivation, equation (2) results directly from the single assumption that solutions to the moment equations can be expressed as the product of a temporal scaling function and a spatial similarity function. For constant α, A and g, the solution to equation (2) is (taking only the positive root as physically realizable)

$$h(t) = \alpha A g t^2 + 2(\alpha A g h_0)^{1/2} t + h_0, \tag{3}$$

where h_0 is a virtual starting thickness, which depends on how long it takes for the flow to become self-similar, which in turn depends on the spectrum of initial perturbations. Alternatively, if $t = 0$ is assigned to the point when the flow first achieves self-similarity, then h_0 corresponds to the thickness of the mixing region at that time.

Numerous attempts to measure α have been made by plotting h versus Agt^2 and fitting a line to the most visually pleasing portion of the data. Dimonte *et al.*[20,21] provide a history of such attempts and note that as grid resolutions have increased, α has decreased. More grid points enable simulations to run further in time, as measured by the number of 'bubble mergers'. The availability of ever more powerful computers has led to a somewhat ironic state of affairs, in that agreement between simulations and experiments is worse today than it was several decades ago. Dimonte *et al.* and Ramabrabhu *et al.*[22] attribute the growing disparity to long wavelength modes in the experiments, which are not present in the more recent simulations. Although this is almost certainly true, there is a more fundamental reason for the decrease in α from recent simulations. Dividing equation (3) by Agt^2 yields

$$\alpha = \frac{h}{Agt^2} - \left(\frac{\alpha h_0}{Ag}\right)^{1/2} \frac{2}{t} - \frac{h_0}{Agt^2}. \tag{4}$$

Figure 4 compares α computed directly from equation (2) against α computed from just the first term in equation (4). The former method yields a nearly constant value at moderate Reynolds number, whereas the latter method suffers from the t^{-1} dependence of the missing terms. The two measures have not come into agreement even by the end of the simulation. The $h/(Agt^2)$ (blue) curve in Fig. 4 illustrates why larger simulations generate lower values of α. Fitting a line to h versus Agt^2 essentially picks off an α from the blue curve corresponding to a time near the end of the simulation. RTI growth exhibits linear as well as quadratic behaviour, with the spectrum of initial perturbations determining the persistence of the linear term.

A close examination of the similarity measure of α (black curve in Fig. 4) reveals a slow rise for $t/\tau > 19$ (Re $> 10^4$). It is tempting to ignore this small effect or attribute it to statistical noise; however, there is a compelling reason why α may indeed exhibit a weak Reynolds number dependence, even in the fully self-similar regime. The reason relates to the energy budget and mixing effects.

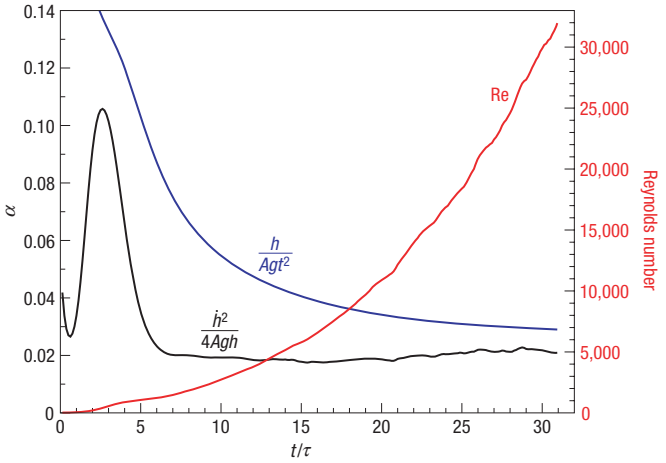

Figure 4 Comparison of measurement techniques for RTI growth parameter, α, including Reynolds number (Re) dependence. The mixing layer thickness (h) and its growth rate ($\dot{h}$) are normalized by the Atwood number (A), gravity (g) and time (t). The blue curve illustrates why standard curve-fitting techniques have yielded lower α values as simulations have reached higher effective Reynolds numbers. In contrast, the similarity method (black curve) is more robust.

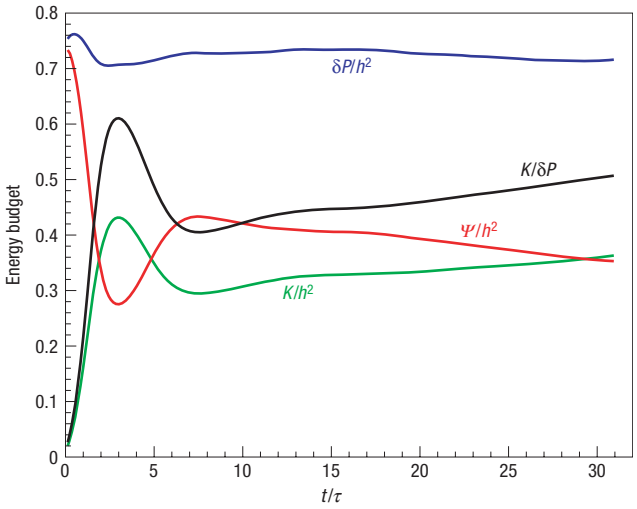

Figure 5 RTI energy budget. Released potential energy (δP) scales with the square of the width of the mixing region (h^2); however, kinetic energy (K) and dissipated energy (Ψ) do not exhibit the same scaling. Consequently, the ratio of kinetic to released potential energy ($K/\delta P$) exhibits a gradual rise at late time. All dimensional terms in this figure are scaled in terms of gravity (g), the density of the light fluid (ρ_L), and the horizontal area of the computational domain (L^2).

ENERGY BUDGET

The potential energy released into the flow is

$$\delta P(t) = \int_V [\rho(\mathbf{x},0) - \rho(\mathbf{x},t)] g z \, \mathrm{d}V, \tag{5}$$

the kinetic energy present in the flow is

$$K(t) = \frac{1}{2}\int_V \rho u_i u_i \, \mathrm{d}V$$

and the energy dissipated into heat is

$$\Psi(t) = \int_0^t \int_V \rho\epsilon \, \mathrm{d}V \, \mathrm{d}t',$$

where ϵ is the dissipation rate (equation (19)) and $V = L^3$ is the domain volume with $\mathrm{d}V = \mathrm{d}x\,\mathrm{d}y\,\mathrm{d}z$. The ratio of kinetic energy to released potential energy is plotted in Fig. 5. The $K/\delta P$ ratio exhibits a shallow but steady rise for $t/\tau > 19$ or $\mathrm{Re} > 10^4$. The Alpha Group[20] demonstrated that $\alpha \propto K/\delta P$ and report a constant value of $K/\delta P = 0.46 \pm 0.04$ from their numerical simulations. The Alpha-Group simulations were conducted at grid resolutions up to $256 \times 256 \times 512$ points. Simulations at that resolution are able to reach $t/\tau \approx 13$ before the flow feels the periodic boundaries[19,23]. It is perhaps an unfortunate coincidence that $K/\delta P$ seems nearly flat at that time.

The rise in $K/\delta P$ can be understood by examining the mechanical energy equation. Taking the dot product of velocity with the momentum equation (14), and dropping the negligible volume-expansion work term, $p\partial u_i/\partial x_i$, yields

$$\frac{\partial}{\partial t}\left(\frac{1}{2}\rho u_i u_i\right) + \frac{\partial}{\partial x_j}\left(\frac{1}{2}\rho u_i u_i u_j + p u_j - u_i \tau_{ij}\right) = -\rho g w - \tau_{ij}\frac{\partial u_i}{\partial x_j}. \tag{6}$$

Because there is no net flux through the boundaries, integrating equation (6) over the domain volume removes all the pure divergence terms on the left-hand side, resulting in

$$\frac{\mathrm{d}K}{\mathrm{d}t} = -\int_V \rho g w \, \mathrm{d}V - \int_V \tau_{ij}\frac{\partial u_i}{\partial x_j}\, \mathrm{d}V. \tag{7}$$

Substituting $\tau_{ij} = 2\rho\nu S_{ij}$, where S_{ij} is the symmetric strain-rate tensor (equation (20)) and decomposing $\partial u_i/\partial x_j$ into symmetric and anti-symmetric parts yields

$$\tau_{ij}\frac{\partial u_i}{\partial x_j} = 2\rho\nu S_{ij}S_{ij} = \rho\epsilon. \tag{8}$$

Furthermore,

$$w \equiv \frac{\mathrm{D}z}{\mathrm{D}t} \equiv \left(\frac{\partial}{\partial t} + u_j\frac{\partial}{\partial x_j}\right) z \tag{9}$$

and

$$\int_V \rho g \frac{\mathrm{D}z}{\mathrm{D}t}\, \mathrm{d}V = \frac{\mathrm{d}}{\mathrm{d}t}\int_V \rho g z \, \mathrm{d}V \tag{10}$$

thus equation (7) becomes

$$\frac{\mathrm{d}K}{\mathrm{d}t} = -\frac{\mathrm{d}}{\mathrm{d}t}\int_V \rho g z \, \mathrm{d}V - \int_V \rho\epsilon \, \mathrm{d}V. \tag{11}$$

Integrating equation (11) from 0 to t with stationary domain boundaries yields

$$K(t) = \delta P(t) - \Psi(t). \tag{12}$$

Inserting a piecewise-linear expression for the horizontally averaged density, $\langle\rho\rangle$, into equation (5) yields $\delta P = (\rho_H - \rho_L) g h^2/6$ (ref. 20). We have normalized equation (12) by h^2 and plotted the three terms in Fig. 5. Energy production does indeed follow h^2 scaling; however, kinetic energy and dissipation do not. At

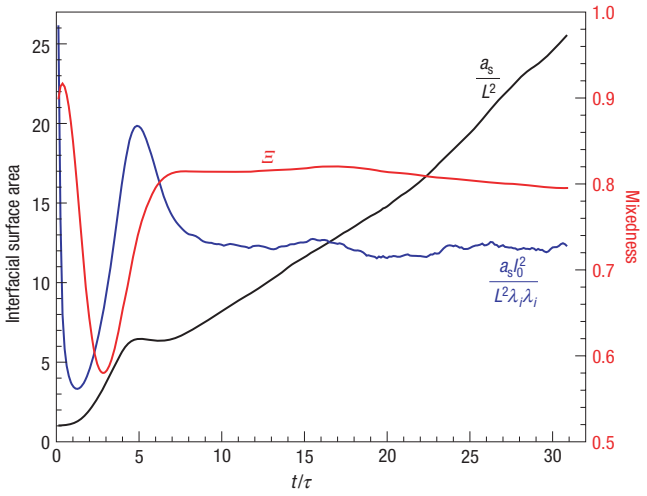

Figure 6 Interfacial surface area and state of mixing in RTI flow. The area of the equimolar ($X = 1/2$) surface (a_s) is shown normalized both by the horizontal area of the flow domain (L^2) and by the square of the Taylor microscale ($\lambda_i\lambda_i$). The Taylor microscale is related to the curvature of the fluid interface. The (l_0^2) factor corresponds to the square of the dominant wavelength of initial perturbations. The mixedness parameter, Ξ, is unity for completely homogenized (diffused) fluids and zero for completely segregated (immiscible) fluids.

higher Reynolds numbers, dissipation lags production, such that kinetic energy grows faster than $\dot{h}^2$. Potential energy is released into the mixing layer at scales $\sim h$ and dissipated into heat at scales $\sim\eta$. As the separation between h and η increases ($h/\eta \propto t^{9/4}$, ref. 18), the cascade time lengthens. The non-stationarity of the turbulent cascade is such that most of the kinetic energy present in the layer is that which has been most recently deposited. It takes roughly an eddy turnover time ($\sim K/\dot{\Psi}$) for Ψ to respond to the energy deposited by δP; during this time, more energy is deposited than previously existed. (The energy dilemma is analogous to the cosmological expansion; to wit, we cannot see the universe as it exists today but only how it was in the far past.) If the rise in $K/\delta P$ persists beyond the window of this simulation, there may be serious consequences for supernovae and other RTI flows at extremely high Reynolds numbers. By assuming $u' \approx \dot{h}$ and lumping all the kinetic energy into the vertical component, Dimonte *et al.*[20] derived an upper bound of $K/\delta P = 12\alpha = 1$ or $\alpha = 0.083$. The observed ratio of horizontal to vertical kinetic energy from both our simulation and the Alpha-Group simulations is $\approx$0.58. Accounting for this partition, Dimonte *et al.* give an upper bound on α of $\approx$0.053. Hence, high Reynolds number RTI flows could exhibit roughly double the growth rate of simulations in which effective Reynolds numbers (real or numerical) are limited by grid resolution.

MIXING EFFECTS

The non-constant nature of $K/\delta P$ has a subtle effect on the mixing rate. A 'mixedness' parameter, Ξ, (equation (22)) is plotted in Fig. 6, wherein a shallow but persistent drop-off is observed for $t/\tau > 19$ ($\mathrm{Re} > 10^4$). As the flow evolves, it entrains pure fluids in ever larger parcels and mixes them at ever finer scales. The turbulent cascade gets longer with increasing Reynolds number and pure fluids spend more time inside the layer before they get mixed. Pure fluids exert greater buoyancy forces than mixed fluids; hence, the growth rate increases as the stabilizing effect of mixing decreases. The pronounced drop in Ξ for $t/\tau \leq 3$ is caused by coherent mushroom-like structures engulfing large parcels of pure fluid. The subsequent steep rise for $3 < t/\tau < 7$ corresponds to rapid break-up and stirring of the pure-fluid parcels as the structures begin to merge.

Mixing also limits the rate of growth of interfacial surface area between the fluids. Figure 6 shows two different normalizations of the surface area versus time. Once again, a change in slope is observed around $t/\tau = 19$ or $\mathrm{Re} = 10^4$. The normalization with Taylor microscale is flat because λ_i is related to wrinkling of the interfacial isosurface. Although the dependence of surface area and other flow properties on the Reynolds number is weak, the net effect may become large when extrapolated to Reynolds numbers many orders of magnitude higher than the DNS.

ASTROPHYSICAL IMPLICATIONS

The dependence of interfacial surface area on the Reynolds number has important implications for type-Ia supernovae, where $\mathrm{Re} \sim 10^{14}$ (ref. 24). RTI wrinkling of the flame greatly increases the net burning rate, owing to the fact that, in the flamelet regime, rates of reaction and heat release in any given volume are proportional to $S_l a_f$, where S_l is the laminar flame speed and a_f is the flame's surface area[9,17]. The actual surface area will greatly exceed the cross-sectional area, L^2, when the flame is highly wrinkled. In typical large eddy simulations (LES), a_f is grossly under-represented; hence, $S_l a_f$ is replaced by $S_t L^2$, where S_t is an effective turbulent flame speed provided by a subgrid-scale model. For strong turbulence in the flamelet regime, $S_t \propto u'$, where u' is independent of S_l (ref. 25). In the thin flame limit,

$$S_t/S_l = a_f/L^2;$$

hence, the area ratio in Fig. 6 mirrors the turbulent-to-laminar flame speed ratio (assuming $S_l \ll u'$) (ref. 15).

A successful model for S_t in type-Ia supernovae must: (i) produce enough energy to unbind the star, (ii) create observed amounts of intermediate-mass elements and (iii) eject materials with velocities matching Doppler shifts of spectral line emissions. Initial burning must be slow, to pre-expand the star, but then become fast, to produce large amounts of high-velocity intermediate-mass elements. To meet all of these conditions, the turbulent flame must accelerate from S_l to roughly 30% of the speed of sound[26]. This final speed approximately corresponds to the maximum Mach number that a compressible RTI will produce[11]. Therefore, it seems prudent to ensure that the model for S_t faithfully reproduces RTI physics before invoking other schemes to increase the burning rate, such as multi-point ignition, background turbulence from thermal convection and/or deflagration-to-detonation transition[9,26].

In the early part of a supernova LES, RTI growth can occur entirely below the filter width ($\bar{\Delta}$), as seen in the dispersion relation (equation (1)). SGS models that rely on a cascade of energy from resolved-scale eddies typically assume a filter cutoff in the inertial range of the energy spectrum. The question then is what to do when the energy spectrum peaks at a wavenumber above the filter cutoff? For example, in the absence of pre-existing turbulence and for sufficiently small perturbations, h could be less than $\bar{\Delta}$, even for a flame that has propagated many grid cells out from the origin. In formulating a flame speed model that accounts for this possibility, we can decompose u' into a resolved component directly computable on the LES grid, u'_{res}, and an unresolved subgrid-scale component, u'_{sgs}. The components are empirically related to $\dot{h}$ in the DNS by

$$u' = \left(u'^2_{\mathrm{res}} + u'^2_{\mathrm{sgs}}\right)^{1/2} \approx 1.2\dot{h}. \qquad (13)$$

For the more general case, including reaction and expansion effects, Schmidt *et al.*[10,27] provide a partial differential equation for u'_{sgs} and use the flame speed model[15,25,28]

$$S_t = \left(S_l^2 + \frac{4}{3} u'^2_{sgs} \right)^{1/2}.$$

Their dynamical equation for u'_{sgs} contains contributions associated with the turbulence cascade as well as an 'Archimedean force' associated with SGS buoyancy. We suggest that equations (2) and (13) could be used as a consistency check on the SGS buoyancy model for the incompressible non-reacting case.

Alternatively, equation (2) could be integrated in a supernova LES, along with the governing equations, by varying A and g according to the mean radius of the flame and the temporal expansion of the star. Expansion of the coordinate system could be taken into account by augmenting $\dot{h}$ with a factor corresponding to dilatation of the burning region. In any event, a flame speed model consistent with equation (2) should provide slower initial burning with greater flame acceleration than steady-state models, wherein S_t is constrained by the transverse dimension of a computational test box[29] or the LES grid spacing[9].

Our results suggest that proper representation of fine-scale initial perturbations is essential for obtaining the correct growth history. Even if the overall flow is not sensitive to details of the solution during the early transition period, this nascent stage sets the virtual starting length scale, h_0, in equation (3), which in turn determines the timing for the onset of rapid late-time growth ($t > \sqrt{h_0/\alpha A g}$). If h_0 is related to a pre-existing thermal convection spectrum then large-scale perturbations may be warranted. However, if h_0 is determined by small-scale wrinkles generated by the Landau–Darrieus instability[30], then imposing large-scale perturbations above $\bar{\Delta}$ seems guaranteed to produce the wrong burning rate.

Finally, we must contend with the fact that the growth rate, mixing rate, kinetic energy content and interfacial surface area of RTI all exhibit weak Reynolds number dependencies for $\mathrm{Re} > 10^4$. Consequently, significant uncertainly remains as to the ultimate state of the flow.

METHODS

GOVERNING EQUATIONS AND THEIR SOLUTION

The governing equations for two incompressible miscible fluids in an accelerating frame of reference are[23]:

$$\frac{\partial \rho}{\partial t} + u_j \frac{\partial \rho}{\partial x_j} = -\rho \frac{\partial u_j}{\partial x_j} = \rho \frac{\partial}{\partial x_j}\left(\frac{D}{\rho} \frac{\partial \rho}{\partial x_j} \right),$$

$$\frac{\partial \rho u_i}{\partial t} + \frac{\partial \rho u_i u_j}{\partial x_j} = \rho g_i - \frac{\partial p}{\partial x_i} + \frac{\partial \tau_{ij}}{\partial x_j}, \tag{14}$$

where

$$\tau_{ij} = \mu \left[\frac{\partial u_i}{\partial x_j} + \frac{\partial u_j}{\partial x_i} - \frac{2}{3} \delta_{ij} \frac{\partial u_k}{\partial x_k} \right].$$

Here t is time, $x_j = (x, y, z)$ is distance, ρ is density, $u_i = (u, v, w)$ is velocity, p is pressure, $g_i = (0, 0, -g)$ is acceleration, D is mass diffusivity, μ is shear viscosity and τ_{ij} is the viscous stress tensor.

The equations are solved using a hybrid spectral-Padé scheme for spatial derivatives, combined with a pressure-projection method for temporal integration. The scheme is designed to minimize numerical dissipation, while maximizing the range of scales that are well resolved by the discrete derivatives. Verification and validation tests of the numerical algorithm have previously been reported[19,23]. The solution constitutes a direct numerical simulation in the sense that all scales of motion, including the viscous and diffusive scales, are completely resolved; that is, energy dissipation is physical rather than numerical.

SIMULATION DETAILS

The flow begins from a quiescent state, with heavy fluid of density $\rho_H = 3$ placed atop light fluid of density $\rho_L = 1$ ($A = 1/2$). An initially diffuse interface (spanning roughly 6 grid points) exists at $z = 0$, with a gaussian spectrum of perturbations imposed around mode 96 (32 points per wavelength). Grid spacing is uniform ($\Delta x = \Delta y = \Delta z = \Delta$); gravity ($g$), diffusivity ($D$), and kinematic viscosity ($\nu = \mu/\rho$) are all constant, with the grid Grashof number ($2gA\Delta^3/\nu^2$) and the Schmidt number (ν/D) both set to unity. For the above parameters, $\psi \approx 1 + 0.375k\delta$ with $\delta \approx 6\Delta$. Equation (1) predicts that the most rapidly growing perturbation occurs at mode number 74 (wavelength $\approx 41\Delta$) and that mode numbers greater than 214 are stabilized (wavelengths $< 14\Delta$).

The DNS was carried out on a $3{,}072 \times 3{,}072 \times N_z$ vertically expanding grid with periodic boundaries in x and y. At the beginning of the simulation, N_z was 256; by the end, N_z reached a value of 3,072, thus forming a cubic domain. A potential flow solution was matched to the intermediate z-boundaries, with impermeable free-slip conditions imposed at the top and bottom of the final cube. Tests of the z-boundary conditions were carried out on domains with different aspect ratios to ensure the matching procedure had no artificial influence on the flow. The simulation ran for just over two weeks on the IBM BlueGene/L machine, first for 4.3 days on 32,768 nodes (half machine), then for 10.2 days on 65,536 nodes (full machine).

CHARACTERISTIC LENGTH- AND TIME SCALES

Relevant length- and time scales for the flow are set by gravity and the initial perturbations. A characteristic horizontal wavelength of any variable, $\phi(x, y, z, t)$, is

$$l_\phi(t) \equiv 2\pi \frac{\int_0^{k_{max}} E_\phi(k, 0, t)/k \, dk}{\int_0^{k_{max}} E_\phi(k, 0, t) \, dk}, \tag{15}$$

where $k = \sqrt{k_x^2 + k_y^2}$ is the magnitude of horizontal wavevectors associated with an annulus in Fourier space, $k_{max} = \pi/\Delta$ (corresponding to a maximum mode number of 1,536) and $E_\phi(k, z, t)$ is the two-dimensional energy spectrum of ϕ fluctuations. The dominant initial wavelength is $l_0 = l_\rho(0)$; therefore, a natural timescale is

$$\tau \equiv \left(\frac{l_0}{Ag} \right)^{1/2}. \tag{16}$$

For this simulation, $l_0 = 32\Delta$ and $\tau = 8\sqrt{\Delta/g}$.

With homogeneity in x and y, ensemble averages (denoted by angle brackets) are equivalent to horizontal integrals, that is, for any variable $\phi(x, y, z, t)$ in a box with $L \times L$ horizontal dimensions,

$$\langle \phi \rangle (z, t) = \frac{1}{L^2} \int_0^L \int_0^L \phi(x, y, z, t) \, dx \, dy.$$

A Taylor microscale in the ith direction can be defined as

$$\lambda_i(z, t) = \left[\frac{\langle u_i^2 \rangle}{\langle (\partial u_i / \partial x_i)^2 \rangle} \right]^{1/2} \quad \text{(no sum on } i\text{)}. \tag{17}$$

Similarly, a Kolmogorov microscale in the ith direction can be defined as

$$\eta_i(z, t) = \left(\frac{\nu^3}{\epsilon_i} \right)^{1/4}, \tag{18}$$

where

$$\epsilon_i(z, t) = 15\nu \left\langle \left(\frac{\partial u_i}{\partial x_i} \right)^2 \right\rangle \quad \text{(no sum on } i\text{)}$$

is the dissipation rate. For isotropic turbulence,

$$\epsilon_i = \epsilon \equiv 2\nu S_{ij} S_{ij}, \tag{19}$$

where

$$S_{ij} = \frac{1}{2} \left(\frac{\partial u_i}{\partial x_j} + \frac{\partial u_j}{\partial x_i} \right) \tag{20}$$

is the strain-rate tensor[31]. With horizontal isotropy, it is convenient to combine x and y components, namely, $\lambda_{xy} = (\lambda_x + \lambda_y)/2$ and $\eta_{xy} = (\eta_x + \eta_y)/2$.

GROWTH RATE AND MIXING DEFINITIONS

The rate of growth of the mixing layer can be robustly defined in terms of entrainment of pure-fluid mole fractions. The mole fraction of heavy fluid is

$$X = \frac{\rho - \rho_{\mathrm{L}}}{\rho_{\mathrm{H}} - \rho_{\mathrm{L}}},$$

and the mole fraction of mixed fluid is

$$X_{\mathrm{m}}(X) = \begin{cases} 2X & \text{if } X \leq 1/2 \\ 2(1-X) & \text{if } X > 1/2 \end{cases}.$$

The width of the mixing region is defined as the thickness of mixed fluid that would result if the entrained fluids were perfectly homogenized in x and y, that is,

$$h \equiv \int_{-\infty}^{\infty} X_{\mathrm{m}}(\langle X \rangle)\, \mathrm{d}z. \tag{21}$$

Thus, h is an entrainment length, derived from the volumes of pure fluids entering the turbulent mixing region. The state of mixing within the layer is quantified as the ratio of mixing length to entrainment length, that is,

$$\Xi \equiv \frac{\int_{-\infty}^{\infty} \langle X_{\mathrm{m}} \rangle\, \mathrm{d}z}{h}. \tag{22}$$

The visual width, H, defined as the range in z for which $0.01 \leq \langle X \rangle \leq 0.99$, is observed to be $\approx 2.4h$. The flow Reynolds number is defined as

$$\mathrm{Re} \equiv \frac{H\dot{H}}{\nu}. \tag{23}$$

Received 31 March 2006; accepted 28 June 2006; published 23 July 2006.

References

1. Rayleigh, L. Investigation of the character of the equilibrium of an incompressible heavy fluid of variable density. *Proc. R. Math. Soc.* **14,** 170–177 (1883).
2. Taylor, G. I. The instability of liquid surfaces when accelerated in a direction perpendicular to their plane. *Proc. R. Soc. London A* **201,** 192–196 (1950).
3. Bateman, G. *MHD Instabilities* (MIT Press, Cambridge, Massachusetts, 1979).
4. Petrasso, R. D. Rayleigh's challenge endures. *Nature* **367,** 217–218 (1994).
5. Taleyarkhan, R. P. *et al.* Evidence for nuclear emissions during acoustic cavitation. *Science* **295,** 1868–1873 (2002).
6. Burrows, A. Supernova explosions in the universe. *Nature* **403,** 727–733 (2000).
7. Zingale, M., Woosley, S. E., Rendleman, C. A., Day, M. S. & Bell, J. B. Three-dimensional numerical simulations of Rayleigh-Taylor unstable flames in type Ia supernovae. *Astrophys. J.* **632,** 1021–1034 (2005).
8. Zingale, M., Woosley, S. E., Bell, J. B., Day, M. S. & Rendleman, C. A. The physics of flames in type Ia supernovae. *J. Phys. Conf.* **16,** 405–409 (2005).
9. Gamezo, V. N., Khokhlov, A. M., Oran, E. S., Chtchelkanova, A. Y. & Rosenberg, R. O. Thermonuclear supernovae: Simulations of the deflagration stage and their implications. *Science* **299,** 77–81 (2003).
10. Schmidt, W., Niemeyer, J. C., Hillebrandt, W. & Röpke, F. K. A localised subgrid scale model for fluid dynamical simulations in astrophysics: II. Application to type Ia supernovae. *Astron. Astrophys.* **450,** 283–294 (2006).
11. Mellado, J. P., Sarkar, S. & Zhou, Y. Large-eddy simulation of Rayleigh-Taylor turbulence with compressible miscible fluids. *Phys. Fluids* **17,** 076101 (2005).
12. Chandrasekhar, S. The character of the equilibrium of an incompressible heavy viscous fluid of variable density. *Proc. Camb. Phil. Soc.* **51,** 162–178 (1955).
13. Duff, R. E., Harlow, F. H. & Hirt, C. W. Effects of diffusion on interface instability between gases. *Phys. Fluids* **5,** 417–425 (1962).
14. Timmes, F. X. & Woosley, S. E. The conductive propagation of nuclear flames. I. Degenerate C + O and O + Ne + Mg white dwarfs. *Astrophys. J.* **396,** 649–667 (1992).
15. Peters, N. *Turbulent Combustion* (Cambridge Univ. Press, Cambridge, 2000).
16. Dimotakis, P. E. The mixing transition in turbulence. *J. Fluid Mech.* **409,** 69–97 (2000).
17. Nomoto, K., Iwamoto, K. & Kishimoto, N. Type Ia supernovae; their origin and possible applications in cosmology. *Science* **276,** 1378–1382 (1997).
18. Ristorcelli, J. R. & Clark, T. T. Rayleigh-Taylor turbulence: Self-similar analysis and direct numerical simulations. *J. Fluid Mech.* **507,** 213–253 (2004).
19. Cook, A. W., Cabot, W. & Miller, P. L. The mixing transition in Rayleigh-Taylor instability. *J. Fluid Mech.* **511,** 333–362 (2004).
20. Dimonte, G. *et al.* A comparative study of the turbulent Rayleigh-Taylor instability using high-resolution three-dimensional numerical simulations: The Alpha-Group collaboration. *Phys. Fluids* **16,** 1668–1693 (2004).
21. Dimonte, G., Ramaprabhu, P., Youngs, D. L., Andrews, M. J. & Rosner, R. Recent advances in the turbulent Rayleigh-Taylor instability. *Phys. Plasmas* **12,** 056301 (2005).
22. Ramaprabhu, P., Dimonte, G. & Andrews, M. J. A numerical study of the influence of initial perturbations on the turbulent Rayleigh-Taylor instability. *J. Fluid Mech.* **536,** 285–319 (2005).
23. Cook, A. W. & Dimotakis, P. E. Transition stages of Rayleigh-Taylor instability between miscible fluids. *J. Fluid Mech.* **443,** 69–99 (2001).
24. Woosley, S. E., Wunsch, S. & Kuhlen, M. Carbon ignition in type Ia supernovae: An analytic model. *Astrophys. J.* **607,** 921–930 (2004).
25. Damköhler, G. Der einfluß der turbulenz auf die flammengeschwindigkeit in gasgemischen. *Z. Elektrochem.* **46,** 601–652 (1940).
26. Hillebrandt, W. & Niemeyer, J. C. Type Ia supernova explosion models. *Annu. Rev. Astron. Astrophys.* **38,** 191–230 (2000).
27. Schmidt, W., Niemeyer, J. C. & Hillebrandt, W. A localised subgrid scale model for fluid dynamical simulations in astrophysics: I. Theory and numerical tests. *Astron. Astrophys.* **450,** 265–281 (2006).
28. Pocheau, A. Scale invariance in turbulent front propagation. *Phys. Rev. E* **49,** 1109–1122 (1994).
29. Khokhlov, A. M., Oran, E. S. & Wheeler, J. C. Scaling in buoyancy-driven turbulent premixed flames. *Combust. Flame* **105,** 28–34 (1996).
30. Röpke, F. K., Niemeyer, J. C. & Hillebrandt, W. On the small-scale stability of thermonuclear flames in type Ia supernovae. *Astrophys. J.* **588,** 952–961 (2003).
31. Tennekes, H. & Lumley, J. L. *A First Course in Turbulence* (MIT Press, Cambridge, Massachusetts, 1972).

Acknowledgements

We wish to thank B. J. Miller, M. L. Welcome and P. L. Williams for assistance with code optimization, and H. R. Childs for help in creating Figs 1 and 6. This work was carried out under the auspices of the US Department of Energy by the University of California Lawrence Livermore National Laboratory under contract No. W-7405-Eng-48.
Correspondence and requests for materials should be addressed to W.H.C. or A.W.C.

Competing financial interests

The authors decline to provide information about competing financial interests.